ADVANCES FUNCTIONAL MATERIALS 28.11 (2018): 1704434

DOI: http://doi.org/10.1002/adfm.201704434

DOI: 10.1002/ ((please add manuscript number))
Article type: Full Paper

Optomagnetic nanoplatforms for in situ controlled hyperthermia

Dirk H. Ortgies, Francisco J. Teran, Uéslen Rocha, Leonor de la Cueva, Gorka Salas, David Cabrera, Alexander S. Vanetsev, Mikhel Rähn, Väino Sammelselg, Yurii V. Orlosvkii, and Daniel Jaque*

Dr. D. H. Ortgies, Dr. U. Rocha, Prof. D. Jaque
Fluorescence Imaging Group, Departamento de Física de Materiales, Facultad de Ciencias, Universidad Autónoma de Madrid, C/ Francisco Tomás y Valiente 7, 28049, Madrid, Spain
E-mail: dirk.ortgies@uam.es

Dr. D. H. Ortgies, Prof. D. Jaque
Instituto Ramón y Cajal de Investigación Sanitaria IRYCIS, Ctra. Colmenar km. 9.100 Madrid, 28034, Spain

Dr. F. J. Teran, Dr. L. de la Cueva, Dr. G. Salas, D. Cabrera
iMdea Nanociencia, Campus Universitario de Cantoblanco, C/ Faraday 9, 28049 Madrid, Spain

Dr. F. J. Teran, Dr. G. Salas
Nanobiotecnología (iMdea Nanociencia), Unidad Asociada al Centro Nacional de Biotecnología (CSIC), 28049 Madrid, Spain

Dr. U. Rocha
Grupo de Fotônica e Fluidos Complexos, Instituto de Física, Universidade Federal de Alagoas, 57072-900 Maceió-AL, Brazil

Dr. A. S. Vanetsev, Prof. Y. V. Orlovskii
A. M. Prokhorov General Physics Institute, Vavilova Str. 38, Moscow 19991, Russia

Dr. A. S. Vanetsev, Dr. M. Rähn, Prof. V. Sammelselg, Prof. Y. V. Orlovskii
Institute of Physics, University of Tartu, W. Ostwaldi Str. 1, Tartu 50411, Estonia

Keywords: hybrid nanostructures, photothermal therapy, magnetic hyperthermia, nanothermometry, luminescence

Magnetic nanoparticles (M:NPs) are unique agents for *in vivo* thermal therapies due to their multimodal capacity for efficient heat generation under optical and/or magnetic excitation. Nevertheless, their transfer from laboratory to the clinic is hampered by the absence of thermal feedback and by the influence that external conditions (e.g. agglomeration, matrix interactions) have on their heating efficiency. Overcoming these limitations requires, first, the implementation of strategies providing thermal sensing to M:NPs in order to obtain *in situ* thermal feedback during thermal therapies. At the same time, M:NPs should be modified so that their heating efficiency will be maintained independent of the environment and the added capability for thermometry. In this work, we present optomagnetic hybrid structures (OMHSs) that simultaneously satisfy these two conditions. Polymeric encapsulation of M:NPs with neodymium-doped nanoparticles (Nd:NPs) results in a hybrid structure capable of subtissue thermal feedback while making the heating efficiency of M:NPs independent from the medium. The potential application of the OMHSs herein developed for fully controlled thermal therapies is demonstrated by an *ex vivo* endoscope-assisted controlled intracoronary heating experiment.

1. Introduction

Hyperthermia as a means to treat pathogens or diseases has been known to mankind over the ages.[1] Due to the systemic nature of classical, non selective, hyperthermia treatments mediated by ultrasound,[2] microwaves[3] or infrared radiation,[4] hyperthermia is not well represented in current medical applications. Conversely, local hyperthermia is increasing in relevance thanks to the progress of nanotechnology and material science. Different types of nanoparticles (NPs) can act as efficient and local nanoheaters (NHts) through remote-activation by e.g. infrared irradiation[5] and/or alternating magnetic fields (H_{AC}),[6] which leads to therapeutic effects through the activation of protein- and DNA-denaturation in the targeted cells or through direct thermal ablation of the cells.[7] The first works reporting the application of NHts in magnetic hyperthermia (MH) date back to the 50s,[6b] and more recently, numerous studies showing the success of proofs of concept and clinical trials have boosted the research interest into them. [6a, 6c, 8] Among these magnetic nanoparticles (M:NPs), iron oxide nanoparticles (IONPs) are the most widely employed.[9] Their success relies on the precise control of their magnetic properties, negligible toxicity and the wide variety of available surface modification methods for providing high colloidal stability in biological media and for anchoring biomolecules.[10] Over the last years M:NPs have also emerged as efficient light-to-heat converters, showing great potential for the development of new *in vivo* thermal therapies of malign tumors by using infrared irradiation as external stimulus.[11] Furthermore, *in vivo* experiments also demonstrated the synergetic benefits of performing simultaneous (optical plus magnetic) activation of M:NP-mediated heating.[5] The combination of both heating mechanisms makes M:NPs unique minimally-invasive thermal agents.

Actually, the successful translation of M:NPs into the clinic is hampered by two inherent drawbacks. First, the significant reduction of the magnetic heating generated by M:NPs inside biological matrices, and second, the lack of thermal feedback. The first drawback is related to the influence of biological matrices on the magnetic properties of M:NPs. Recent works show that they increase NP clustering inside cells or tissues, resulting in relevant modifications of their magnetic response (including magnetic heating, and imaging signals).[12] Indeed, it was found that magnetic dipolar interactions and nanoparticle immobilization are responsible (to different extents) for a reduction of the magnetic heating efficiency up to 90%. This makes it difficult to control the heat dose during an *in vivo* M:NP-based hyperthermia treatment. The second drawback stems from M:NPs currently not offering any intrinsic property that can provide real time thermal feedback during a thermal treatment. Most of the *in vivo* demonstrations of M:NPs-based thermal therapies aim for thermal control through temperature measurements with infrared thermal cameras. These often fail to give an accurate subcutaneous / intratissue thermal reading as they can only access surface (skin) temperature that could differ significantly, for example, from the actual intratumoral temperature.[8c, 13] As a consequence, inaccurate therapies and undesired and harmful side effects con occur. Overcoming these two limitations implies the development of a modification that would equip M:NPs with a contactless subcutaneous thermal feedback functionality while preserving their heating efficiency in biological tissues.

Providing M:NPs with thermal control can be achieved through combination with luminescent nanothermometers (LNThs); nanoparticles whose luminescence is strongly temperature-dependent in the physiological range (20 - 60 ºC). A great variety of LNThs was successfully employed for temperature control in *in vitro* and *in vivo* thermal therapies.[14] Subcutaneous thermal feedback requires the use of LNThs working in the so-called biological windows (BWs). BWs are spectral ranges, covering from 700 up to 1870 nm, in which tissues become partially transparent so that large optical penetration depths are achieved.[15] Furthermore, accurate and consistent luminescence thermometry requires the use of LNThs capable of multiparametric temperature determination (i.e. showing different temperature dependent spectral parameters).[16] In this case the combination of luminescence thermometry and neural network recognition has made luminescence thermal sensing with thermal and time resolutions as good as 0.2 °C and 10 ns possible.[17] Thermal control of M:NPs by luminescence thermometry has already been successfully demonstrated, combining M:NPs with rare earth compounds or organic dyes emitting in the visible domain,[18] limiting their employability for *in vivo* applications that demand high penetration into tissues. Furthermore, in previous cases temperature determination was based on a single parameter analysis, reducing the robustness of the thermal feedback. The combination of M:NPs and multiparameter infrared LNThs for subtissue accurate thermal sensing is therefore still a challenge that has not yet been accomplished.

In order to satisfy these conditions (multiparametric thermal sensitivity in the infared BWs), neodymium-doped LaF_3 nanoparticles (Nd:NPs) appear of special relevance due to their already demonstrated capability for providing real time and accurate thermal control during *in vivo* thermal therapies.[14e, 19] Furthermore, Nd:NPs were also recently demonstrated to be outstanding thermal controllers of NHts and a “green” hydrothermal microwave treatment (HTMW) technique demonstrated to significantly enhance their fluorescence brightness allowing their use as infrared contrast agents.[16, 20] Thus, the combination of both M:NPs and Nd:NPs into a single nanostructure would allow for accurate and real time thermal feedback in M:NP-based thermal therapies under optical and/or magnetic excitation. Such a desired structure is schematically drawn in **Figure 1**. Among the alternatives to combine M:NPs and Nd:NPs into a single nanostructure, encapsulation with the polymer poly(lactic-*co*-glycolic acid) **(**PLGA) emerges as especially relevant.[21] PLGA encapsulation would ensure good biocompatibility allowing for the safe *in vivo* application of the hybrid structure.[21-22] Furthermore, polymeric encapsulation randomly immobilizes M:NPs, freezing the interparticle distance, i.e. the magnetic dipolar interactions, which should preserve the magnetic heating efficiency. Although polymeric encapsulation of M:NPs with Nd:NPs could simultaneously solve the two limitations of M:NPs as thermal agents, it is still an unexplored solution.

In this work we have designed and synthetized hybrid nanostructures containing simultaneously both M:NPs in the form of IONPs and Nd:NPs. Hybrid nanostructures were obtained by joint encapsulation of both M:NPs and Nd:NPs with the biocompatible polymer PLGA via a typical double emulsion method and decorated on the surface with a polyethylenglycol ligand in order to improve water dispersability.[21, 23] The developed optomagnetic hybrid nanostructures (OMHSs) combine the heating capabilities of the M:NPs with the multiparametric sensing ability of the Nd:NPs. A series of experiments were conducted to demonstrate the benefits of polymeric encapsulation not only in terms of thermal feedback but also in maintaining the heating efficiency of the M:NPs. Finally, the potential application of the OMHSs for *in situ* controlled thermal therapies is explored by the design and development of simple *ex vivo* experiments.

2. Results and Discussion

After the synthesis of the OMHSs was successfully conducted as described in the Experimental Section a detailed morphological analysis was performed. **Figure 2(a)** includes a TEM image of a single OMHS. In this image, the presence of individual nanoparticles within a polymeric capsule is evidenced. This polymeric capsule has a diameter of ≈ 300 nm on the TEM grid although the average hydrodynamic diameter (D_H) of the OMHSs dispersed in water was 185 ± 76 nm (see Section 2 and **Figure S1** in the Supporting Information). This is quite similar to the size of previously reported hybrid polymeric nanostructures.[22] **Figure 2(a)** reflects the nanoparticle encapsulation but it does not clarify the content nor the joint encapsulation of Nd:NPs and M:NPs in the polymeric capsule. High-angle annular dark-field imaging (HAADF) compositional imaging experiments were performed to verify the capsule composition and the results are shown in **Figures 2(b), (c), and (d)**. In particular, **Figure 2(c)** and **2(d)** correspond to the HAADF images obtained in terms of the Lanthanum and Iron content. These two images denote the simultaneous presence of both LaF_3:Nd and γ-Fe_2O_3 NPs within the polymeric capsule. Additionally, the average composition of the OMHSs was determined by inductively coupled plasma - optical emission spectrometry (ICP-OES) and thermogravimetric analysis (TGA) (for details see the Supporting Information and **Figure S2**) and resulted in 20 % iron oxide, 50 % LaF_3 and 30 % organic material (PLGA and surface coatings).

Further evidence of joint encapsulation is shown in **Figure 3**. **Figure 3(a)** depicts the optical image of the OMHSs' dispersion (1 mg/mL) in phosphate-buffered saline (PBS). The dispersion appears homogeneous with a light brown color, attributed to the distribution of the polymeric capsules. **Figure 3(b)** shows the same colloidal dispersion when a magnet is placed in close proximity. The dispersion becomes transparent and it is evident that all the encapsulates have been attracted towards the magnet due to the magnetic force exerted over the encapsulated γ-Fe_2O_3 NPs. The good magnetic properties of the encapsulated IONPs are also reflected in the magnetization cycles of the OMHSs at room temperature (see **Figure S3**). Additional evidence of the joint encapsulation of M:NPs and Nd:NPs in the polymer is shown in the infrared fluorescence images of the cuvette in the absence and presence of the magnet (see **Figures 3(c)** and **(d)**). Optical excitation was performed by an 808 nm diode laser and the image was acquired by using an InGaAs infrared camera combined with a longpass filter so that the infrared fluorescence image is unequivocally correlated with the presence of OMHSs in the suspension. **Figure 3(c)** shows the infrared fluorescence image of the suspension in absence of the magnet. This image suggests an homogeneous distribution of luminescent Nd:NPs. On the other hand, in presence of the magnet, luminescence is only detected in its proximities, denoting that all the Nd:NPs moved in unison with the M:NPs and no emission from "free" Nd:NPs was observed, i.e. all the Nd:NPs are within OMHSs. Thus, **Figures 3(a)-(d)** constitute a solid evidence of the simultaneous encapsulation of both Nd:NPs and M:NPs within the OMHSs.

Figure 3(e) shows the optical extinction coefficient of a colloidal solution of OMHSs in PBS. For the sake of comparison, the absorption extinction spectrum of PBS is also included. The difference between the two extinction spectra included in **Figure 3(e)** evidences that the OMHSs present a non-vanishing extinction cross section in the 500-1400 nm spectral range. Indeed, the extinction cross section of OMHSs increases noticeably at shorter wavelengths in very good accordance with the extinction spectra reported for a great variety of magnetic structures.[5, 11, 24] At this point it should be noted that the narrow absorption lines of Nd:NPs are not observed in the extinction spectrum of OMHSs, thus indicating that optical extinction is mainly given by the presence of M:NPs within the polymeric capsules. The absence of sharp bands in the extinction coefficient of OMHSs is an outstanding point since it suggests that the absorption coefficient and, hence, the optical-to-heat conversion efficiency will not be as dependent on the particular excitation wavelength as it happens with rare-earth-based or plasmonic NHts.[19a, 25]

Figure 3(f) shows the room temperature emission spectrum as obtained when a dispersion of OMHSs was optically excited with an 808 nm diode laser. The emission spectrum is constituted by three emission bands centered at around 900, 1060 and 1340 nm that are unequivocally correlated to the $^4F_{3/2} \rightarrow {}^4I_{9/2}$, $^4I_{11/2}$, and $^4I_{13/2}$ transitions, respectively. There is no evidence of the presence of additional emission bands neither due to the polymeric capsule nor to the magnetic nanoparticles. This fact reveals Nd:NPs as the unique fluorescent unit within the OMHSs. Furthermore, the shape of the emission bands generated by the Nd:NPs within the OMHSs is virtually the same as that of colloidal Nd:NPs.[26] This suggest that neither the encapsulation procedure nor the proximity of M:NPs have any relevant influence on the fluorescence properties of the Nd:NPs.

Finally, in order to evaluate the influence of the encapsulation procedure on the magnetic heating efficiency of M:NPs, **Figure 3(g)** shows the values of the specific absorption rate (SAR) obtained for differently coated (oleic acid (OA) and dimercaptosuccinic acid (DMSA)) IONPs. **Figure 3(g)** also includes the SAR values obtained for OMHSs at two different aggregation levels denoted as OMHSs and OMHSs-BSA, with D_H values of 209 nm and 503 nm but similar size distributions (poly dispersity index (PDI) of 0.26 and 0.22, respectively). The modification of D_H was achieved through addition of bovine serum albumin (BSA) as explained in detail in the Experimental Section. The observed SAR values were obtained with a field frequency and intensity of 100 kHz and 24 kA/m, respectively. As shown in the figure, the SAR values remain identical for OA and DMSA coated IONPs, but significantly drop (~50%) when IONPs are integrated into OHMSs. This drop can be understood in terms of the interparticle interaction inside the OMHS encapsulate. [27] Such dipolar interacting phenomena are clearly observed when DMSA-coated IONPs are intentionally aggregated (see **Figure S4**) and their hydrodynamic size is increased from 99 to 208 nm. Their SAR values decrease 35 % due to the increase of the intra-aggregate magnetic dipolar interactions. The SAR value is also 35% reduced when the viscosity is 100-fold increased, demonstrating that IONP immobilization decreases the heat losses. In this way, one can understand that the SAR value of OMHSs decreases more than 40% with respect to DMSA-coated IONPs, as a consequence of intra-aggregate dipolar interactions and particle immobilization inside the OMHS capsule. However, no remarkable differences of SAR values are observed when the D_H of OMHSs is intentionally increased from 208 to 503 nm, underlining the invariability of magnetic heating of OMHSs when aggregation is induced. This can be understood in terms of the preservation of the interparticle distance inside the OMHSs capsule, resulting in no significant effects when another capsule approaches. In summary, **Figure 3** reveals the encapsulation with PLGA as an efficient technique to join M:NPs and Nd:NPs into a single nanostructure while preserving their desired optical and magnetic properties.

Figure 4 summarizes the results obtained from the experiments conducted to evaluate the contactless thermal sensing capacity of OMHSs. Details about the experimental procedure used for thermal calibration can be found in the Experimental Section. **Figure 4(a)** shows a detail of the $^4F_{3/2}\rightarrow{}^4I_{9/2}$ emission band of Nd^{3+} ions as obtained at two different temperatures. Relevant changes are observed. Firstly, there is a noticeable spectral change. The ratio $R = I_1 / I_2$ between the emitted intensities at 862.5 and 864 nm (denoted as I_1 and I_2, respectively) increases with temperature. This increment, shown in **Figure 4(b)**, can be used for ratiometric thermal sensing. The temperature dependence of the ratiometric thermal sensitivity, S_R that is defined as $S_R = R^{-1} \cdot dR\ dT^{-1}$ is also shown in **Figure 4(b)**. At 30 °C the ratiometric thermal sensitivity has been found to be close to 0.4% $°C^{-1}$, which is indeed comparable to that recently published for optimized LaF_3:Nd NPs,[19c] although it is lower than the ratiometric thermal sensitivities reported for other luminescent nanoparticles.[28] Nevertheless, previous studies demonstrated that this thermal sensitivity is high enough to allow for accurate subtissue remote thermal measurements.[19b] In addition to their ratiometric thermal sensitivity, OMHSs possess an additional thermal reading possibility through the spectral shift of their emission line at around 864 nm. As can be observed in **Figure 4(c)** this emission line suffers a linear temperature induced redshift at a rate of 0.002 nm $°C^{-1}$. This double thermal sensitivity is an outstanding feature that converts the OMHSs into robust thermal sensors since it allows for a double-check of the thermal readout. Note that, as it is explained in the Experimental Section, the reduced spectral shift of the 864 nm line does not imply that thermal measurements based on this spectral shift require a high resolution spectrometer. Indeed, peak position is determined by fitting the emission spectra to three Gaussian peaks and it was found that the use of a spectrometer with a resolution of 0.2 nm is enough to determine temperature from the spectral shift at 864 nm. Regarding the physical mechanisms causing the temperature induced spectral changes, they have been explained in previous papers. Briefly, the temperature induced change in the ratio between emission lines can be correlated with a thermal re-distribution between the sub-stark levels of the $^4F_{3/2}$ and $^4I_{9/2}$ electronic levels of the Neodymium ions in the LaF_3 network. At the same time the red-shift of the emission line was unequivocally associated with thermally induced strains in the Nd^{3+} environment that occur as a result of electron-phonon interaction**.[ACS Nano, 2013, 7 (2), pp 1188–11999]**

Having successfully characterized the OMHSs, their applicability was to be demonstrated in *ex vivo* experiments. **Figure 5** shows a schematic representation of the experimental set-up designed in this work to demonstrate the suitability of our OMHSs for subtissue heating under optical or magnetic activation with simultaneous contactless thermal feedback (more details about this set-up can be found in the Experimental Section). Briefly, powdered OMHSs are deposited inside a quartz tube placed in the coil gap, where a homogenous H_{AC} (100 kHz and 0-32 kA m^{-1}) is applied. The OMHSs are optically excited with an 808 nm diode laser coupled to a multicore fiber. The fluorescence generated by the OMHSs was collected by the same multicore fiber and was spectrally analyzed by a high resolution monochromator. The sample was irradiated with excitation light 5 min before spectrum acquisition in order to achieve the required dynamical equilibrium temperature for thermal measurements. Details about thermal stabilization can be found in Supporting Information. This set-up allows us to place a tissue between the optical fiber and the OMHSs. Information about the thermal resolution achieved in this experimental configuration can be found in Supporting Information.

Figure 6(a) shows the emission spectra generated by the powdered OMHSs in the absence of any applied magnetic field and tissue as obtained for two different 808 nm laser powers. As can be observed increasing the laser power from 10 mW up to 380 mW leads to a clear modification in the emission spectrum. The intensity ratio R is increased and the emission line at 864 nm is simultaneously redshifted, both indicating a local temperature increment inside the OMHSs. Similar results were obtained when a biological tissue (chicken breast, 3 mm thick) was placed between the end of the multicore-fiber and the powdered OMHSs. Figure 6(b) shows the OMHSs temperature increment as a function of the 808 nm laser power obtained in the absence and presence of the tissue. Figure 6(b) includes the temperature increments calculated from the analysis of the changes induced in the intensity ratio R (denoted as ΔT_R) as well as those calculated from the spectral shift of the 864 nm emission line (denoted as ΔT_λ). In the presence and in the absence of the tissue, both thermometry procedures lead to equal temperature increments, supporting the correctness of the measurements. At this point, it should be noted that the presence of the tissue reduces the magnitude of the laser-induced heating in the OMHSs. The rate at which temperature increases in respect to laser power was found to decrease from 400 down to 39 °C W^{-1} when the OMHSs were placed under the tissue. Such drastic reduction was, indeed, expected due to the extinction of the 808 nm laser beam when crossing the tissue. The extinction coefficient of breast tissue at 808 nm was estimated to be close to 8 cm^{-1}. Applying the Beer-Lambert law and taking into account the tissue thickness used in our experiments (3 mm) the 808 nm laser intensity reaching the OMHSs beneath the tissue is estimated to be only 10% of the optical power delivered by the diode laser.[29] This is in good agreement with the reduction experimentally observed in the heating rates which is close to one order of magnitude. Similar measurements were also performed by placing a 2 mm thick skin tissue (from chicken) as well as from a 3 mm thick sample of bold (obtained from a sacrificed mouse). We found that the optical power, after passing the skin tissue and blood sample, was reduced down to 15 % and 4 % of its incident value, respectively. This can be compared with the expected reduction that can be calculated by the Beer-Lambert law and the effective attenuation coefficients of skin and blood at 808 nm reported in the literature (8 and 17 cm^{-1}, respectively).**[doi:10.1038/nnano.2009.326 and https://doi.org/10.1111/1523-1747.ep12479191]** Using these values Beer-Lambert law predicts a transmitted laser power that is 20 and 3% of the incident laser power for skin and blood, respectively. These are also in reasonable good agreement with the experimental data.

Figure 6(c) shows the emission temperature generated by the OMHSs for a fixed 808 nm excitation power (2.5 W) as obtained in absence (blue line) of any magnetic field and when a H_{AC} (100 kHz and 32 kA m^{-1}) was applied (red line). These thermal sensing experiments were performed in the presence and absence of the tissue. A detailed inspection of both spectra reveals that when applying the alternating magnetic field, the intensity ratio R slightly increases and this is accompanied by a small red-shift of the emission line at around 864 nm. These two facts reveal the magnetic field-induced heating of OMHSs. An analysis of both the intensity ratio and spectral shift allowed us to determine the OMHSs temperature increment as a function of the intensity of the alternating applied magnetic field. The results obtained in the presence and the absence of the tissue are included in **Figure 6(d)**. Again both ratiometric and spectral analysis of the emission spectrum leads to virtually the same thermal reading. Temperature increment induced in the OMHSs were found to increase linearly with the intensity of the magnetic field as it was, indeed, expected and observed in previous works.[18b-c] For the maximum field intensity applied by our generator (32 kA m^{-1}) the temperature increment induced within the OMHSs was found to be close to 10±1 °C. In order to check for the correctness of this value we recorded the temperature increment by using an infrared thermal camera. With this camera, due to its reduced spatial resolution, the temperature increment obtained corresponds to the average temperature increment in the whole sample of OMHSs. On the other hand, the temperature increment obtained by luminescence nanothermometry corresponds to the average temperature within the polymeric encapsulate (the Nd:NPs nanothermometers are within the OMHSs). **Figure 6(e)** shows the infrared thermal image of the OMHSs in absence of any applied magnetic field. As expected, no temperature contrast is observed and the OMHSs are at the same temperature as the thermostatic bath in which the magnetic coils are immersed. **Figure 6(f)** shows the thermal image when an alternating magnetic field of 32 kA m^{-1} was applied. In this case, the temperature of the OMHSs is significantly different from that of the thermostatic bath. Thermal images revealed a temperature increment of 11 °C that is virtually the same as that determined by luminescence nanothermometry. This fact indicates that, in this particular case, there is no significant difference between the temperature increments at the nanoscale, i.e. induced inside the encapsulates, and the macroscopic average temperature increments induced over a large sample. This in turn, suggest the presence of an efficient thermal diffusion within the polymeric capsule and between adjacent encapsulates. At this point these results can be compared to those obtained by R. Piñol et al. who found small differences between the nanoscale and bulk temperature increments caused by a colloidal solution of magnetic nanoparticles.[18a] This discrepancy can be understood by recalling that in our case we are dealing with a solid sample of OMHSs so that thermal diffusion is expected to be larger than in an aqueous solution due to the presence of solid-liquid interfaces that could induce relevant thermal impedances. In any case, the good agreement between the thermal reading provided by luminescent nanothermometers and infrared thermal camera reveals the robustness of the structure here proposed for obtaining accurate thermal monitoring of magnetic nanoparticles. **Figure 6(d)** also reveals that the temperature increment induced in the OMHSs by the alternating magnetic field is not affected by the presence of the tissue. This varies from the observation for laser induced heating, and was expected due to the superior penetration of magnetic fields into tissues when compared to 808 nm laser radiation. When measuring the subtissue magnetic field induced heating of our OMHSs, the attenuation of 808 nm laser radiation only affects the signal to noise ratio of the measured spectrum (and hence the uncertainty of the thermal reading) but not the magnitude of heating as, in this case, it is given by the intensity of magnetic field that is not affected by the presence of the tissue. From data included in **Figure 6(d)** we can estimate a magnetic field induced heating rate in our OMHSs close to 0.31 °C m kA^{-1}. This can now be compared to the magnetic-induced heating rates reported for single M:NPs. A. Riedinger and co-workers found that the heating rate, for M:NPs in an aqueous solution, is strongly dependent on the distance at which it is measured in respect to the M:NP. It was as large as 5 °C m kA^{-1} (with a frequency of 334 kHz) at the surface of the M:NP decreasing down to 0.63 °C m kA^{-1} for distances of 2 nm from the M:NP.[18c] Therefore, the heating rate of our OMHSs is comparable to the heating rate found in the past for single M: NPs but at moderate field conditions (100 kHz and 32 kA m^{-1}, instead of 334.5 kHz and 8-16 kA m^{-1}).

At this point we should note that thermal measurements were obtained after analyzing the luminescence generated by OMHSs after passing through the tissue and being partially scattered by it. At this point we state that scattering would be, indeed, a problem if thermal reading would be achieved through a single intensity analysis. But in our case we are dealing with a ratiometric analysis in which temperature is determined from the intensity ratio between two peaks that are very close in wavelength. Thus, scattering would affect both peaks equally and the ratio between them would only carry information about temperature. This also applies for the thermal reading based on the determination of peak wavelength. Note that spectral displacements are very reduced so we can consider that scattering affects all of them equally. Thus, the presence of the tissue induced scattering can affect the level of detected signal but not the thermal information extracted from it.

In order to illustrate the potential of our OMHSs for fully controlled photothermal therapies, we performed an additional *ex vivo* experiment. A powder sample of OMHSs (2 mg) was introduced by a surgical incision into a lamb heart (see arrow in **Figure 7(a)**). Optical excitation of the OMHSs was performed by introducing a multicore fiber into the heart through the pulmonary vein (also indicated in **Figure 7(a)**). The multicore optical fiber was then positioned to maximize the collected fluorescence generated by the OMHSs. Once maximized, the emission spectrum was recorded for different 808 nm laser powers in order to measure the laser induced heating in the coronary wall. **Figure 7(b)** shows the emission spectra obtained for different laser powers ranging from 10 up to 37 mW. The simultaneous increment in the intensity ratio R and the redshift of the 864 nm emission line evidences intracoronary heating due to the presence of OMHSs. The intracoronary temperature increment as a function of the 808 nm laser power, as calculated by using the calibration curves of **Figures 4(b)** and **4(c)**, is shown in **Figure 7(c)**. Once more, both thermal reading approaches lead to similar temperature increments that in turn increase linearly with the 808 nm laser power. Note that the laser induced temperature increment obtained is as large as 50 °C for a moderate laser power of 35 mW. This temperature increment is large enough to induced both hyperthermia and tissue ablation.[30] In addition, the required laser power is moderate, allowing the use of a cheap combination of low power laser diodes and conventional optical fibers. Thus, results included in **Figure 7** reveal the great potential of OMHSs as self-monitored thermal agents in heart therapies where, for instance, real time temperature monitoring would allow accurate control during intracoronary ablation processes that are used for the treatment of cardiac arrhythmias. At this point it should be noted that the temperature uncertainty in the *ex vivo* experiments has been estimated to be 5 °C (mainly due to the reduced signal to noise ratio).[19c] Such thermal accuracy is sufficient when dealing with thermal ablation of tissues (temperature increments of tens of degrees) but it is insufficient to provide thermal control during hyperthermia therapies in which temperature increments do not exceed 10 °C. Further improvement in thermal accuracy would be possible by improving the signal-to-noise ratio of the detection system as well as by applying neural network recognition procedures.

3. Conclusion

In summary, we demonstrated how polymeric encapsulation of magnetic nanoparticles with infrared emitting nanothermometers results in a hybrid nanostructure allowing *in situ* controlled hyperthermia treatment. The synthesized OMHSs keep the properties of both magnetic and luminescent nanoparticles, thereby providing an accurate thermal feedback that results in subtissue thermal control over IONP-mediated heating triggered by either magnetic and/or optical excitation. The encapsulation with PLGA was also found to preserve the magnetic heating efficiency against OMHS agglomeration. Therefore, the OMHSs here developed constitute a robust multifunctional platform capable of fully controlled subcutaneous heating by using either optical or magnetic stimulation. The real potential of our OMHSs was demonstrated by an *ex vivo* intracoronary heating experiment in which subtissue remote heating with contactless thermal feedback was successfully achieved.

Furthermore, the herein described OMHSs could constitute a reference material towards the design of controlled thermal therapies with reduced side effects and superior efficiency in respect to those based on single magnetic nanoparticles. The synergy between optical and magnetic induced heating in magnetic nanoparticles together with the possibility of real time thermal control over them will bring their therapeutic applications closer to the clinic.

4. Experimental Section

Chemicals and solvents were purchased from Sigma Aldrich, Alfa Aesar, Fisher, Acros Organics and if not stated otherwise in the procedure employed as purchased. Rare earths compounds and ammonium fluoride were obtained from Sigma Aldrich in the following purities: $Nd(NO_3)_3 \cdot 5\ H_2O$ (99.999% purity), $La(NO_3)_3 \cdot 6\ H_2O$ (99.999%), and NH_4F (>98%).

Synthesis of Nd-doped lanthanum trifluoride nanoparticles: For the synthesis of LaF_3 nanoparticles doped with 3% Nd^{3+} ions, $La(NO_3)_3 \cdot 6\ H_2O$ (0.485 mmol) and $Nd(NO_3)_3 \cdot 5\ H_2O$ (0.015 mmol) were dissolved in deionized water (15 mL). The solution of rare-earth salts was added dropwise to the NH_4F solution (5 mmol) in deionized water (25 mL) under vigorous stirring. To improve the dispersibility of the obtained nanoparticles, 1 g of biocompatible surfactant polyvinylpyrrolidone (Aldrich, average M_w ~55000) was added to the solutions. The surfactant was added to the rare-earth nitrates solutions before precipitation. The freshly precipitated gel was diluted with deionized water (10 mL) and left stirring for 15 minutes.The solution was transferred into a 100 ml Teflon autoclave and placed under microwave irradiation for 2 hours at 200 °C using a Speedwave Four (Berghof GmbH, Germany) laboratory device (2.45 GHz, 1kW maximum output power). The resulting solution was cooled, centrifuged using a Thermo Scientific Heraeus Multifuge X1 device and washed several times with deionized water. The resulting powder was redispersed in deionized water. The morphology of the particles was determined by TEM (see Supporting Information Section 5 and **Figure S5**) and characterized by powder X-ray diffraction (Supporting Information Section 7 and **Figure S8**).

Synthesis of magnetic nanoparticles: The reaction was carried out by thermal decomposition of Fe(acac)3 (3.53 g, 10 mmol), 1,2-dodecanediol (2.03 g, 10 mmol) and oleic acid (8.47 g, 30 mmol) in 1-octadecene (100 ml), under mechanical stirring.[31] The mixture was first heated to 200 °C and kept at that temperature during 2 h and, then, heated again until reflux for 30 minutes. The mixture was washed with ethanol, centrifuging and with the help of a permanent magnet. Finally, ethanol was removed and the resulting black residue of hydrophobic nanoparticles of magnetite was redispersed in hexane for storing. The mean size of the nanoparticles (determined by TEM, see **Figure S6**) was 21 ± 5 nm. Powder X-ray diffraction (Supporting Information Section 7 and **Figure S9**) confirmed the Fe_3O_4 structure. The iron concentration of the dispersion was measured by Inductively Coupled Plasma Optical Emission Spectrometry (ICP-OES). The aqueous M:NPs used for the encapsulation in this work were prepared by a surface modification procedure with DMSA, as previously described.[32]

Polymeric encapsulation: The OMHS nanocapsules were synthesized via a double-emulsion technique as described previously.[22] PLGA (50:50, MW 19000, 6 mg) was dissolved in dicloromethane (DCM,4 mL) and an aqueous dispersion of superparamagnetic iron oxide nanoparticles (M:NPs, 1 mL, 1 mg/mL) as well as an aqueous dispersion of LaF_3:Nd(3%) (Nd:NPs 1 mL, 40 mg/mL) were added dropwise while sonicating the mixture. The resulting water-in-oil emulsion was added to a solution of polyvinyl alcohol (PVA, 88% hydrolyzed, ≈MW 20–30 000, 200 mg) and DSPE-PEG-folate (0.3 mg) in PBS (8 mL) and sonicated with a tip-sonicator with pulses of up to 20 W for 5 min resulting in a water in-oil-in-water emulsion. In order to induce the hardening and facilitate the precipitation of the encapsulates the dispersion was combined with a solution of PVA (3.6 mg) in PBS (24 mL) and stirred overnight to achieve evaporation of the DCM. The resulting dispersion was centrifuged (Hermle Z206A, Rotor 55, Hermle Labortechnik GmbH) for 30 min at 6000 rpm and the OMHS were three times washed with H_2O and centrifuged for 30 min at 6000 rpm. Afterward the encapsulates were recovered and lyophilized.

Determination of the specific absorption rate: The characterization of the specific absorption rate (SAR) on the studied IONPs was determined from magnetic measurements of the AC hysteresis loops under given H_{AC} (100 kHz and 24 kA m^{-1}). The AC magnetomer employed is a custom-built inductive magnetometer set up developed by the Advanced Instrumentation Unit (iMdea Nanociencia) similar to the one described by Connord, et al.[33] The system quantifies the inductive magnetic signal of IONP dispersions, which is calibrated by comparing magnetization values at given field intensity obtained under AC and quasi-static conditions. Hysteresis loops were determined by averaging ten repetitions. By considering the expression SAR = A×f, where A is the area of the hysteresis loop under alternating magnetic fields, and f is the magnetic field frequency,[34] an average value of SAR and standard deviation were determined.

Variation of the hydrodynamic radius during SAR measurements: For the reduction of the D_H value of the OMHSs, a Bovine Serum Albumin dispersion (5 g/L) was added to the aqueous nanoparticle dispersion to reach the final BSA concentration (0.35 g/L) and iron content (0.5 g/L). The dispersion was sonicated for 5 minutes resulting in a Z-average value of 209 nm (PDI=0.26).

In order to increase the D_H of the DMSA coated IONP, Fetal Bovine Serum (FBS) was added to the dispersion reaching a final fraction of 7 % (V_{FBS}/V_{water}) and an iron content of 0.5 g/L.[35] Immediately afterwards, the Z-average value was 231 nm (PDI=0.31).

Spectroscopic characterization: For spectroscopic characterization a fiber coupled 808 nm laser diode from LIMO was used as an excitation source. The laser fiber was coupled to fiber-based reflection probe (Ocean Optics QR600-7-VIS-NIR). It consists in a fiber bundle of a total of 7 fibers (600 µm diameter). The central fiber is coupled to the 808 nm laser source used for optical excitation. The 6 surrounding fibers are used to collect the luminescence of the sample. The collected luminescence was spectrally analyzed by coupling the exit branch of the bundle to an imaging spectrometer (Horiba iHR320). The luminescence, after dispersion by the grating, was recorded by a CCD array (Horiba Synapse). The spectral resolution of the system is 0.2 nm. Determination of the peak position was performed by fitting the emission spectra to a multiple Gaussian. The power of the 808 nm laser was adjusted by varying the diode current. The ferrule containing both illumination and collecting fibers was made of a ceramic material in order to avoid undesirable heating during magnetic experiments.

For thermal calibration of our OMHSs, these were placed on a temperature controlled stage (Linkam 1200) that allowed to vary the sample temperature from -25 up to 120 °C with a 0.1 °C thermal resolution.

For the acquisition of the fluorescence images included in **Figure 3** the colloidal suspension of OMHSs was illuminated by an uncollimated 808 nm fiber coupled diode. Fluorescence image was acquired by a Peltier cooled InGaAs camera (XEVA 1.7 from

Xenics). A 850 nm longpass filter was used to block the 808 nm laser background. The room temperature extinction spectrum of the colloidal dispersions were measured with a double beam absorption spectrometer (Perkin Elmer Lambda1050).

AC magnetic field generator: A custom-made and designed set-up was employed for generating the H_{AC} enabling the measurement of the temperature raise of the OMHSs. The field conditions available were field frequencies up to 300 kHz and field intensities up to 32 kA/m. The H_{AC} generator is based on a custom made and -designed liquid-cooled ferrite core, coiled with Litz wires, which is part of a LCR resonant circuit. The powder sample (1.2 mg) was placed in a quartz tube that was introduced into the coil.

Supporting Information

Additional experimental details and information on the characterization of the OMHS (TEM, size, compositional analysis, heating efficiency) can be found in the Supporting Information available from the Wiley Online Library or from the author.

Acknowledgements

This work was supported by the Spanish Ministry of Economy and Competitiveness under Projects # MAT2016-75362-C3-1-R, # MAT2015-71806-R and # MAT2013-47395-C4-3-R, the Comunidad de Madrid (NANOFRONTMAG-CM, S2013/MIT-2850), and through the Instituto de Salud Carlos III under Project # PI16/00812. This work has also received funding from European Union's H2020 and FP7 programme (NOCANTHER, GA 685795). D. H. Ortgies is grateful to the Spanish Ministry of Economy and Competitiveness for a Juan de la Cierva scholarship (FJCI-2014-21101) and F. J. Teran for a Ramon y Cajal fellowship (RYC-2011-09617). COST Actions CM1403 and TD1402 (RADIOMAG) are also acknowledged. The synthesis and preliminary testing of the fluorescence properties of the LaF_3:Nd(3%) NPs was supported by Project # 16-12-10077 of the Russian Science Foundation. Non-fluorescent characterization of the OMHSs was supported by projects IUT2-24 and IUT20-54 of the Estonian Ministry of Education and Research. D. H. Ortgies and F. J. Teran contributed equally.

Received: ((will be filled in by the editorial staff))
Revised: ((will be filled in by the editorial staff))
Published online: ((will be filled in by the editorial staff))

References

[1] a) P. Wust, B. Hildebrandt, G. Sreenivasa, B. Rau, J. Gellermann, H. Riess, R. Felix, P. M. Schlag, *Lancet Oncol.* **2002**, *3*, 487; b) D. A. Christensen, C. H. Durney, *J. Microwave Power* **1981**, *16*, 89; c) B. Hildebrandt, P. Wust, O. Ahlers, A. Dieing, G. Sreenivasa, T. Kerner, R. Felix, H. Riess, *Crit. Rev. Oncol. Hematol.* **2002**, *43*, 33; d) R. W. Habash, R. Bansal, D. Krewski, H. T. Alhafid, *Crit. Rev. Biomed. Eng.* **2006**, *34*, 459.

[2] R. Britt, B. Lyons, D. Pounds, S. Prionas, *Med. Instrum.* **1983**, *17*, 6.

[3] J. R. Fike, G. T. Gobbel, T. Satoh, P. R. Stauffer, *Int. J. Hyperthermia* **1991**, *7*, 795.

[4] A. V. A. S. K. H. Wehner, *Int. J. Hyperthermia* **2001**, *17*, 19.

[5] A. Espinosa, R. Di Corato, J. Kolosnjaj-Tabi, P. Flaud, T. Pellegrino, C. Wilhelm, *ACS Nano* **2016**, *10*, 2436.

[6] a) Q. A. Pankhurst, J. Connolly, S. K. Jones, J. Dobson, *J. Phys. D: Appl. Phys.* **2003**, *36*, R167; b) E. A. Périgo, G. Hemery, O. Sandre, D. Ortega, E. Garaio, F. Plazaola, F. J. Teran, *Appl. Phys. Rev.* **2015**, *2*, 041302; c) D. Jaque, L. Martínez Maestro, B. del Rosal, P. Haro-Gonzalez, A. Benayas, J. L. Plaza, E. Martín Rodríguez, J. García Solé, *Nanoscale* **2014**, *6*, 9494.

[7] a) P. M. Krawczyk, B. Eppink, J. Essers, J. Stap, H. Rodermond, H. Odijk, A. Zelensky, C. van Bree, L. J. Stalpers, M. R. Buist, T. Soullié, J. Rens, H. J. M. Verhagen, M. J. O'Connor, N. A. P. Franken, T. L. M. ten Hagen, R. Kanaar, J. A. Aten, *Proc. Natl. Acad. Sci. U. S. A.* **2011**, *108*, 9851; b) K. C. Hadley, M. J. Borrelli, J. R. Lepock, J. McLaurin, S. E. Croul, A. Guha, A. Chakrabartty, *Cell Stress Chaperones* **2011**, *16*, 549; c) H. Wang, J. Fu, Y. Lee, P. Lu, *Mol. Cell. Biol.* **2013**, *33*, 11.

[8] a) M. Johannsen, B. Thiesen, P. Wust, A. Jordan, *Int. J. Hyperthermia* **2010**, *26*, 790; b) K. Maier-Hauff, F. Ulrich, D. Nestler, H. Niehoff, P. Wust, B. Thiesen, H.

Orawa, V. Budach, A. Jordan, *J. Neuro-Oncol.* **2011**, *103*, 317; c) S. Kossatz, R. Ludwig, H. Dähring, V. Ettelt, G. Rimkus, M. Marciello, G. Salas, V. Patel, F. Teran, I. Hilger, *Pharm. Res.* **2014**, *31*, 3274; d) S. Kossatz, J. Grandke, P. Couleaud, A. Latorre, A. Aires, K. Crosbie-Staunton, R. Ludwig, H. Dähring, V. Ettelt, A. Lazaro-Carrillo, M. Calero, M. Sader, J. Courty, Y. Volkov, A. Prina-Mello, A. Villanueva, Á. Somoza, A. L. Cortajarena, R. Miranda, I. Hilger, *Breast Cancer Res.* **2015**, *17*, 66.

[9] a) R. Hergt, S. Dutz, R. Müller, M. Zeisberger, *J. Phys.: Condens. Matter* **2006**, *18*, S2919; b) A. K. Gupta, M. Gupta, *Biomaterials* **2005**, *26*, 3995; c) S. Mornet, S. Vasseur, F. Grasset, E. Duguet, *J. Mater. Chem.* **2004**, *14*, 2161.

[10] a) P. Guardia, R. Di Corato, L. Lartigue, C. Wilhelm, A. Espinosa, M. Garcia-Hernandez, F. Gazeau, L. Manna, T. Pellegrino, *ACS Nano* **2012**, *6*, 3080; b) P. Guardia, A. Riedinger, S. Nitti, G. Pugliese, S. Marras, A. Genovese, M. E. Materia, C. Lefevre, L. Manna, T. Pellegrino, *J. Mater. Chem. B* **2014**, *2*, 4426; c) G. Salas, J. Camarero, D. Cabrera, H. l. n. Takacs, M. Varela, R. Ludwig, H. Dähring, I. Hilger, R. Miranda, M. d. P. Morales, F. J. Teran, *J. Phys. Chem. C* **2014**, *118*, 19985; d) H. Arami, A. Khandhar, D. Liggitt, K. M. Krishnan, *Chem. Soc. Rev.* **2015**, *44*, 8576.

[11] a) H. Peng, J. Tang, R. Zheng, G. Guo, A. Dong, Y. Wang, W. Yang, *Adv. Healthc. Mater.* **2017**, *6*, 1601289; b) S. Shen, S. Wang, R. Zheng, X. Zhu, X. Jiang, D. Fu, W. Yang, *Biomaterials* **2015**, *39*, 67; c) M. Chu, Y. Shao, J. Peng, X. Dai, H. Li, Q. Wu, D. Shi, *Biomaterials* **2013**, *34*, 4078; d) Z. Zhou, Y. Sun, J. Shen, J. Wei, C. Yu, B. Kong, W. Liu, H. Yang, S. Yang, W. Wang, *Biomaterials* **2014**, *35*, 7470.

[12] a) R. Di Corato, A. Espinosa, L. Lartigue, M. Tharaud, S. Chat, T. Pellegrino, C. Ménager, F. Gazeau, C. Wilhelm, *Biomaterials* **2014**, *35*, 6400; b) M. Lévy, C. Wilhelm, M. Devaud, P. Levitz, F. Gazeau, *Contrast Media Mol. Imaging* **2012**, *7*, 373; c) K. Them, *Phys. Med. Biol.* **2017**, *62*, 5623.

[13] H. F. Rodrigues, G. Capistrano, F. M. Mello, N. Zufelato, E. Silveira-Lacerda, A. F. Bakuzis, *Phys. Med. Biol.* **2017**, *62*, 4062.

[14] a) J. S. Donner, S. A. Thompson, C. Alonso-Ortega, J. Morales, L. G. Rico, S. I. C. O. Santos, R. Quidant, *ACS Nano* **2013**, *7*, 8666; b) E. Navarro Cerón, B. del Rosal, F. Ren, A. Benayas, F. Vetrone, D. Ma, F. Sanz-Rodríguez, J. G. Solé, D. Jaque, E. Martín Rodríguez, *Adv. Mater.* **2015**, *27*, 4781; c) U. Rocha, J. Hu, E. M. Rodríguez, A. S. Vanetsev, M. Rähn, V. Sammelselg, Y. V. Orlovskii, J. G. Solé, D. Jaque, D. H. Ortgies, *Small* **2016**, *12*, 5394; d) K. Okabe, N. Inada, C. Gota, Y. Harada, T. Funatsu, S. Uchiyama, *Nat. Commun.* **2012**, *3*, 705; e) B. del Rosal, E. Carrasco, F. Ren, A. Benayas, F. Vetrone, F. Sanz-Rodríguez, D. Ma, Á. Juarranz, D. Jaque, *Adv. Funct. Mater.* **2016**, *26*, 6060; f) C. D. S. Brites, P. P. Lima, N. J. O. Silva, A. Millan, V. S. Amaral, F. Palacio, L. D. Carlos, *Nanoscale* **2012**, *4*, 4799; g) D. Jaque, F. Vetrone, *Nanoscale* **2012**, *4*, 4301; h) X. Zhu, W. Feng, J. Chang, Y. W. Tan, J. Li, M. Chen, Y. Sun, F. Li, *Nat. Commun.* **2016**, *7*, 1.

[15] a) E. Hemmer, A. Benayas, F. Legare, F. Vetrone, *Nanoscale Horiz.* **2016**, *1*, 168; b) R. R. Anderson, J. A. Parrish, *J. Invest. Dermatol.* **1981**, *77*, 13.

[16] K. Kaldvee, A. V. Nefedova, S. G. Fedorenko, A. S. Vanetsev, E. O. Orlovskaya, L. Puust, M. Pärs, I. Sildos, A. V. Ryabova, Y. V. Orlovskii, *J. Lumin.* **2017**, *183*, 478.

[17] L. Liu, K. Zhong, T. Munro, S. Alvarado, R. Côte, S. Creten, E. Fron, H. Ban, M. Van der Auweraer, N. B. Roozen, O. Matsuda, C. Glorieux, *J. Appl. Phys.* **2015**, *118*, 184906.

[18] a) R. Piñol, C. D. S. Brites, R. Bustamante, A. Martínez, N. J. O. Silva, J. L. Murillo, R. Cases, J. Carrey, C. Estepa, C. Sosa, F. Palacio, L. D. Carlos, A. Millán, *ACS Nano* **2015**, *9*, 3134; b) J. Dong, J. I. Zink, *ACS Nano* **2014**, *8*, 5199; c) A.

Riedinger, P. Guardia, A. Curcio, M. A. Garcia, R. Cingolani, L. Manna, T. Pellegrino, *Nano Lett.* **2013**, *13*, 2399.

[19] a) E. Carrasco, B. del Rosal, F. Sanz-Rodríguez, Á. J. de la Fuente, P. H. Gonzalez, U. Rocha, K. U. Kumar, C. Jacinto, J. G. Solé, D. Jaque, *Adv. Funct. Mater.* **2015**, *25*, 615; b) U. Rocha, C. Jacinto, W. F. Silva, I. Guedes, A. Benayas, L. M. Maestro, M. A. Elias, E. Bovero, F. van Veggel, J. A. G. Sole, D. Jaque, *ACS Nano* **2013**, *7*, 1188; c) U. Rocha, C. Jacinto, K. U. Kumar, F. J. López, D. Bravo, J. G. Solé, D. Jaque, *J. Lumin.* **2016**, *175*, 149.

[20] A. Vanetsev, K. Kaldvee, L. Puust, K. Keevend, A. Nefedova, S. Fedorenko, A. Baranchikov, I. Sildos, M. Rähn, V. Sammelselg, Y. Orlovskii, *ChemistrySelect* **2017**, *2*, 4874.

[21] H. Sah, L. A. Thoma, H. R. Desu, E. Sah, G. C. Wood, *Int. J. Nanomed.* **2013**, *8*, 747.

[22] D. H. Ortgies, L. de la Cueva, B. del Rosal, F. Sanz-Rodríguez, N. Fernández, M. C. Iglesias-de la Cruz, G. Salas, D. Cabrera, F. J. Teran, D. Jaque, E. Martín Rodríguez, *ACS Appl. Mater. Inter.* **2016**, *8*, 1406.

[23] R. A. Jain, *Biomaterials* **2000**, *21*, 2475.

[24] R. Pazik, E. Zachanowicz, B. Pozniak, M. Malecka, A. Ziecina, L. Marciniak, *RSC Adv.* **2017**, *7*, 18162.

[25] L. M. Maestro, P. Haro-Gonzalez, B. del Rosal, J. Ramiro, A. J. Caamano, E. Carrasco, A. Juarranz, F. Sanz-Rodriguez, J. G. Sole, D. Jaque, *Nanoscale* **2013**, *5*, 7882.

[26] U. Rocha, K. U. Kumar, C. Jacinto, I. Villa, F. Sanz-Rodríguez, M. del Carmen Iglesias de la Cruz, A. Juarranz, E. Carrasco, F. C. J. M. van Veggel, E. Bovero, J. G. Solé, D. Jaque, *Small* **2014**, *10*, 1141.

[27] J. G. Ovejero, D. Cabrera, J. Carrey, T. Valdivielso, G. Salas, F. J. Teran, *Phys. Chem. Chem. Phys.* **2016**, *18*, 10954.

[28] S. Balabhadra, M. L. Debasu, C. D. S. Brites, L. A. O. Nunes, O. L. Malta, J. Rocha, M. Bettinelli, L. D. Carlos, *Nanoscale* **2015**, *7*, 17261.

[29] T. Durduran, R. Choe, J. P. Culver, L. Zubkov, M. J. Holboke, J. Giammarco, B. Chance, A. G. Yodh, *Phys. Med. Biol.* **2002**, *47*, 2847.

[30] D. E. Haines, D. D. Watson, *Pacing and Clinical Electrophysiology* **1989**, *12*, 962.

[31] a) S. Sun, H. Zeng, *J. Am. Chem. Soc.* **2002**, *124*, 8204; b) B. Pacakova, S. Kubickova, G. Salas, A. R. Mantlikova, M. Marciello, M. P. Morales, D. Niznansky, J. Vejpravova, *Nanoscale* **2017**, *9*, 5129.

[32] G. Salas, C. Casado, F. J. Teran, R. Miranda, C. J. Serna, M. P. Morales, *J. Mater. Chem.* **2012**, *22*, 21065.

[33] V. Connord, B. Mehdaoui, R. P. Tan, J. Carrey, M. Respaud, *Rev. Sci. Instrum.* **2014**, *85*, 093904.

[34] B. Mehdaoui, J. Carrey, M. Stadler, A. Cornejo, C. Nayral, F. Delpech, B. Chaudret, M. Respaud, *Appl. Phys. Lett.* **2012**, *100*, 052403.

[35] A. Aires, D. Cabrera, L. C. Alonso-Pardo, A. L. Cortajarena, F. J. Teran, *ChemNanoMat* **2017**, *3*, 183.

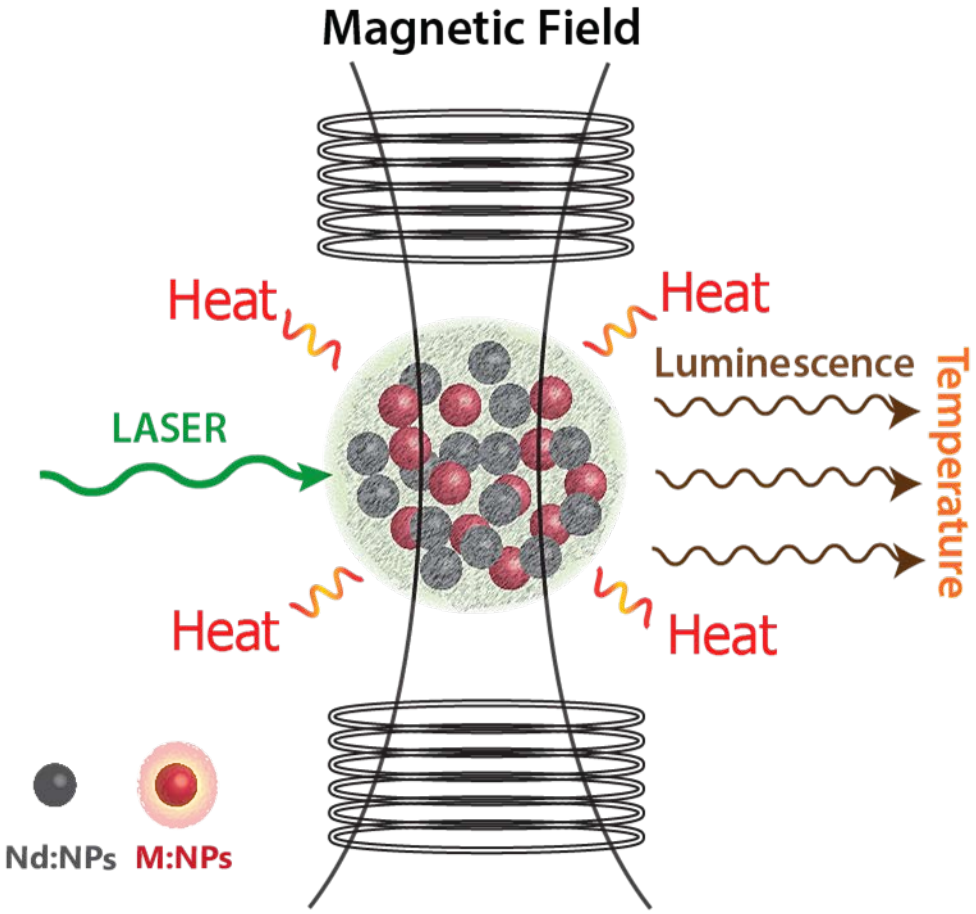

Figure 1. Schematic drawing of the here designed hybrid nanostructure formed by Nd:NPs and M:NPs encapsulated in poly(lactic-*co*-glycolic acid) **(**PLGA) for thermal monitoring of laser and magnetic induced heat generation.

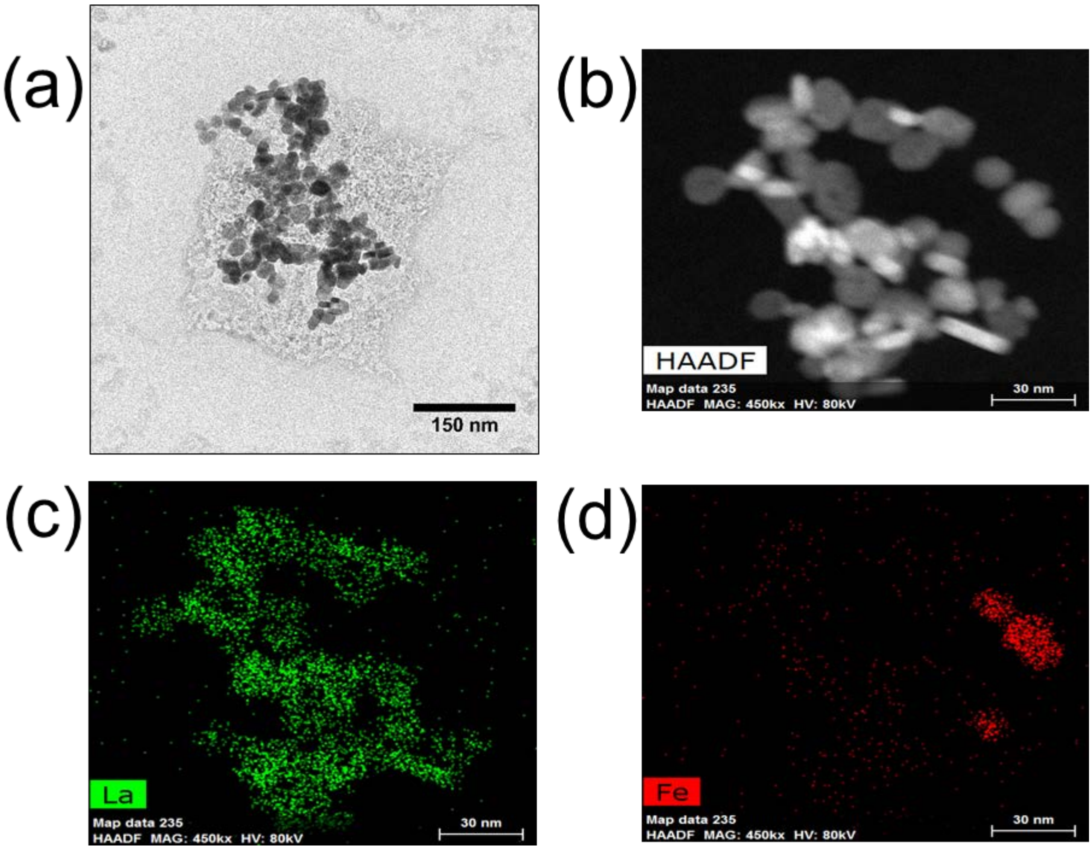

Figure 2. (a) TEM image of a OMHS nanostructure showing the polymer and the encapsulated nanoparties within it. **(b)** HAADF image of a single hybrid nanostructure. **(c)** and **(d)** correspond to the compositional images of the structure included in **(b)** as obtained in terms of the lanthanum and iron content, respectively.

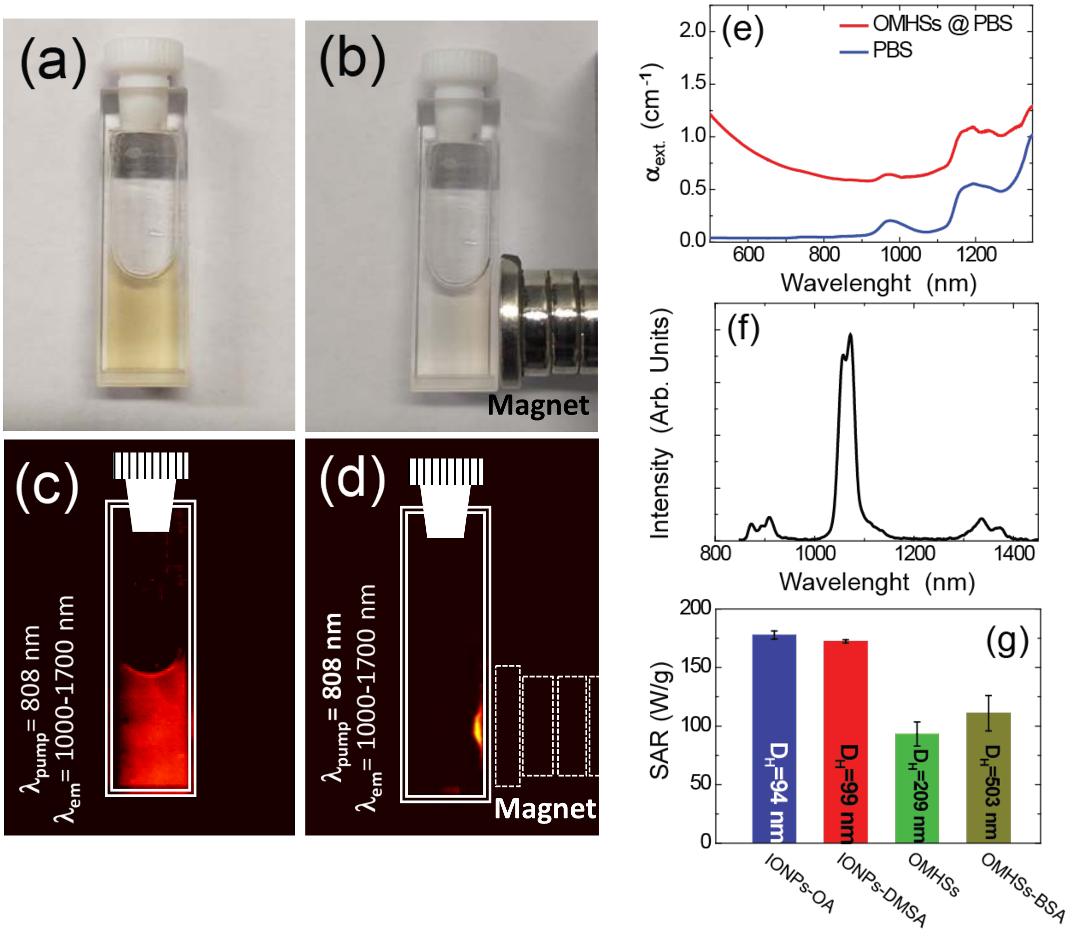

Figure 3. **(a)** and **(b)** correspond to optical pictures of a PBS solution OMHS in absence and presence of a magnet, respectively. Note how the dispersion becomes more transparent due to the motion of OMHSs towards the magnet. **(c)** and **(d)** correspond to the infrared florescence images of the same solution also in absence and presence of a magnet, respectively. The solidary motion of luminescent and magnetic nanoparticles is evidenced. **(e)** Extinction spectrum of the colloidal solution of OMHSs. The extinction spectrum of PBS is also included for comparison. **(f)** Room temperature emission spectrum generated by OMHSs under 808 nm laser excitation. The three characteristic bands of neodymium ions are clearly observed. **(g)** Comparison of SAR values obtained for OA- or DMSA-coated IONPs (labeled as IONPs-OA and IONPs-DMSA, respectively). The SAR values obtained for OMHSs and OMHSs which were aggregated with bovine serum albumin (labeled as OMHSs-BSA) are also included. Each sample was dispersed in liquid media at equal concentrations in iron applying H_{AC} (100 kHz and 24 kA m^{-1}).

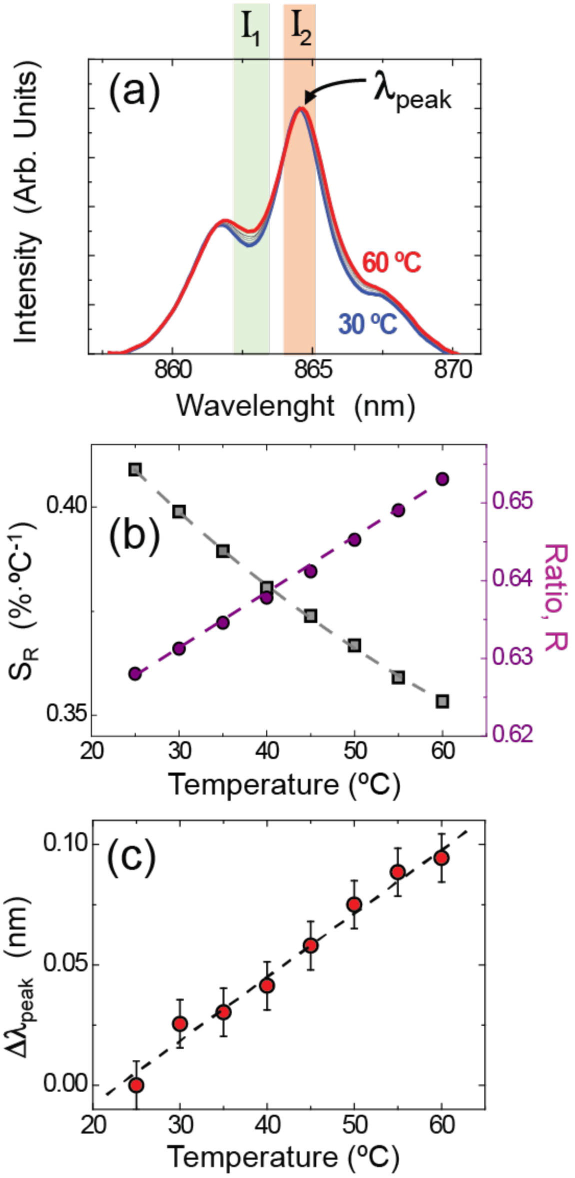

Figure 4. (a) Emission spectra of OMHSs in the 850-870 nm range as obtained for different temperatures (from 30 up to 60 °C). The intensities used for ratiometric thermal measurements are indicated. The peak used for spectral-shift thermal reading measurements is also included. **(b)** Temperature dependence of the intensity ratio $R = I_1/I_2$. The temperature dependence of the ratiometric thermal sensitivity, S_R, is also included. Dots are experimental data and dashed lines are guides for the eyes. **(c)** Temperature dependence of the spectral shift induced in λ_{peak}. Dots are experimental data and dashed line is the best linear fit.

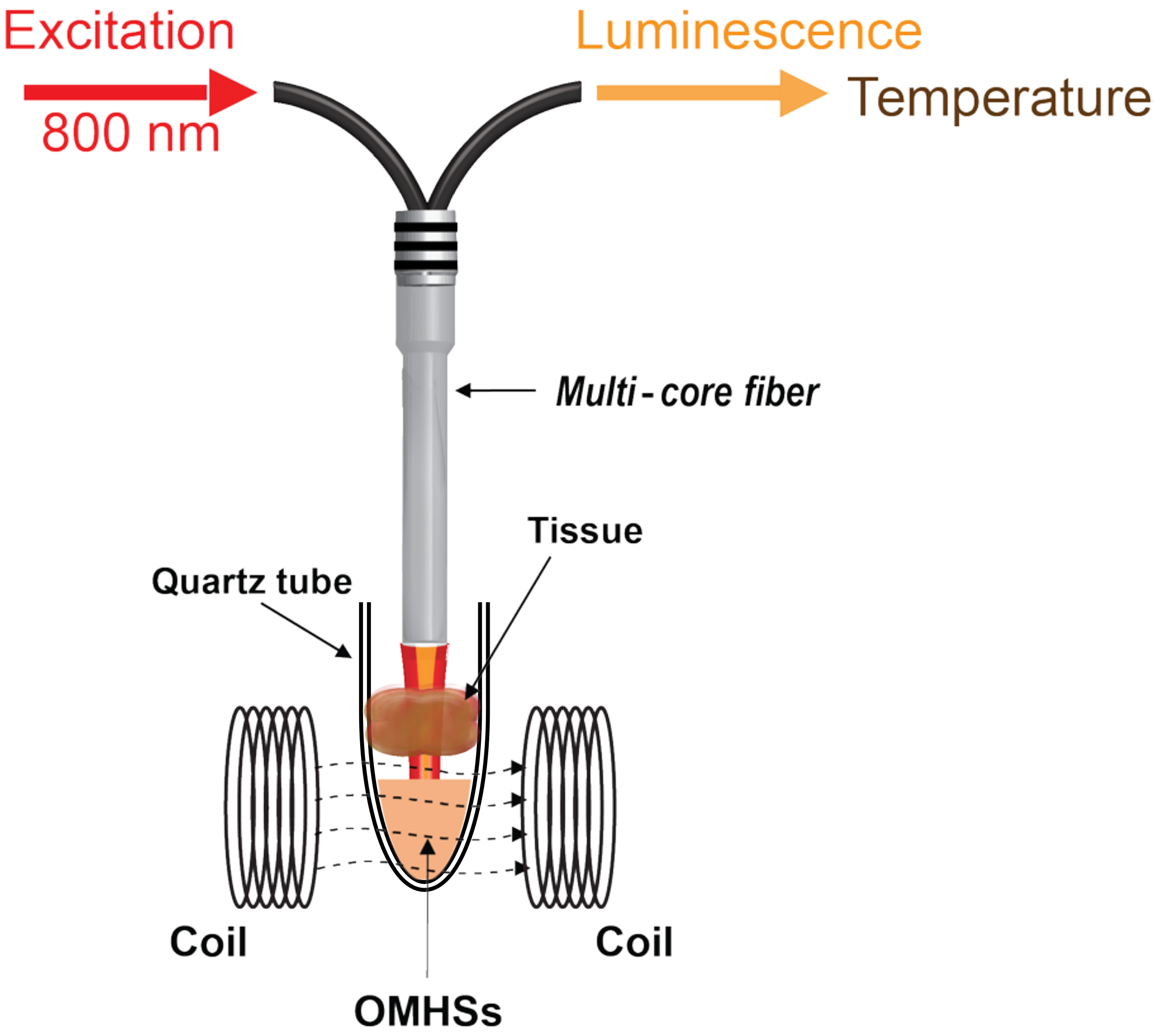

Figure 5. Schematic representation of the experimental set-up designed to demonstrate the ability of OMHSs to provide subtissue thermal sensing during hyperthermia induced by optical or magnetic stimuli.

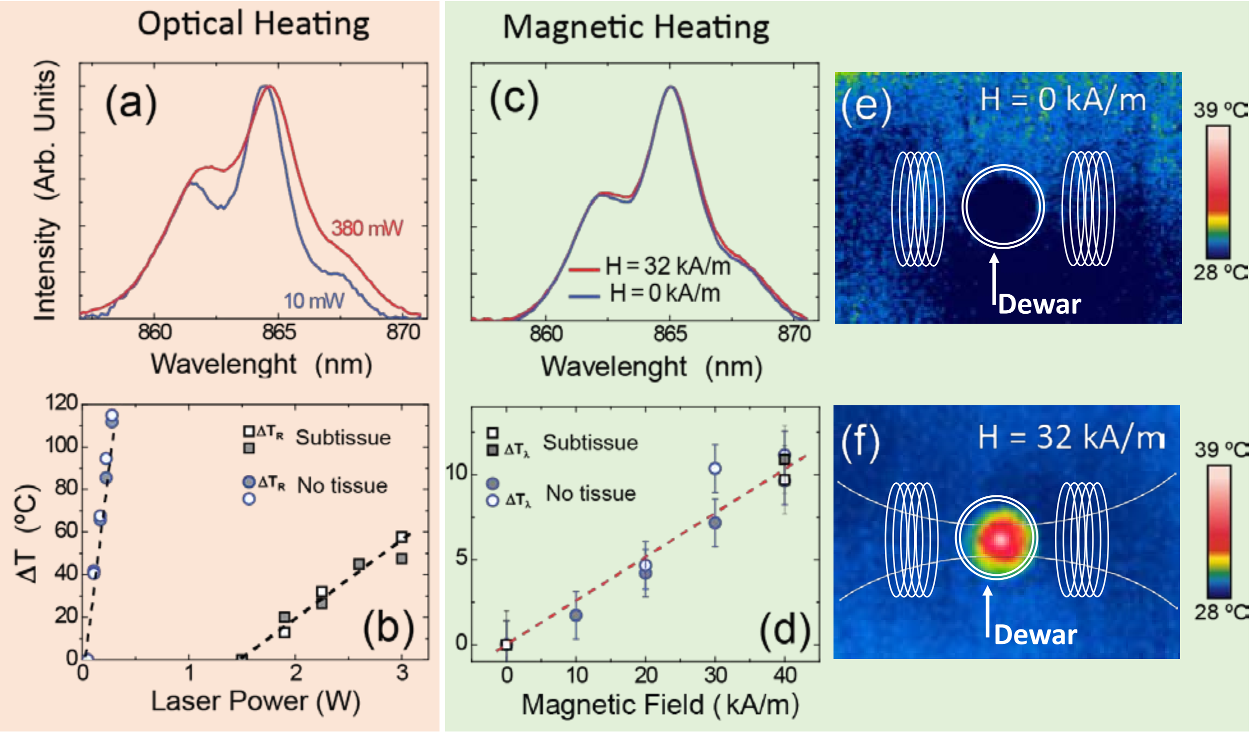

Figure 6. (a) Emission spectra generated by the OMHSs as obtained for two different laser powers: 10 (blue line) and 380 (red line) mW. Spectra were obtained in the absence of any tissue between the excitation/collection fiber and the solid OMHSs. **(b)** Temperature increment induced in the optically excited OMHSs as a function of the laser power as obtained through the ratiometric (ΔT_R) and spectral (ΔT_λ) shift calibration. Results obtained in the presence and absence of tissue are included (circles and squares, respectively). **(c)** Emission spectra generated by the OMHSs as obtained in the absence (blue line) and presence (red line) of an alternating magnetic field (100 kHz and 32 kA m^{-1}). **(d)** Temperature increment induced in the OMHSs as a function of the applied magnetic field in the presence and absence of tissue. Data obtained by using the ratiometric and spectral shift calibrations are included. **(e)** Thermal image of the quartz tube containing the OMHSs in absence of H_{AC}. **(f)** Thermal image of the tube containing the OMHSs in the presence of H_{AC} (100 kHz and 32 kA m^{-1}).

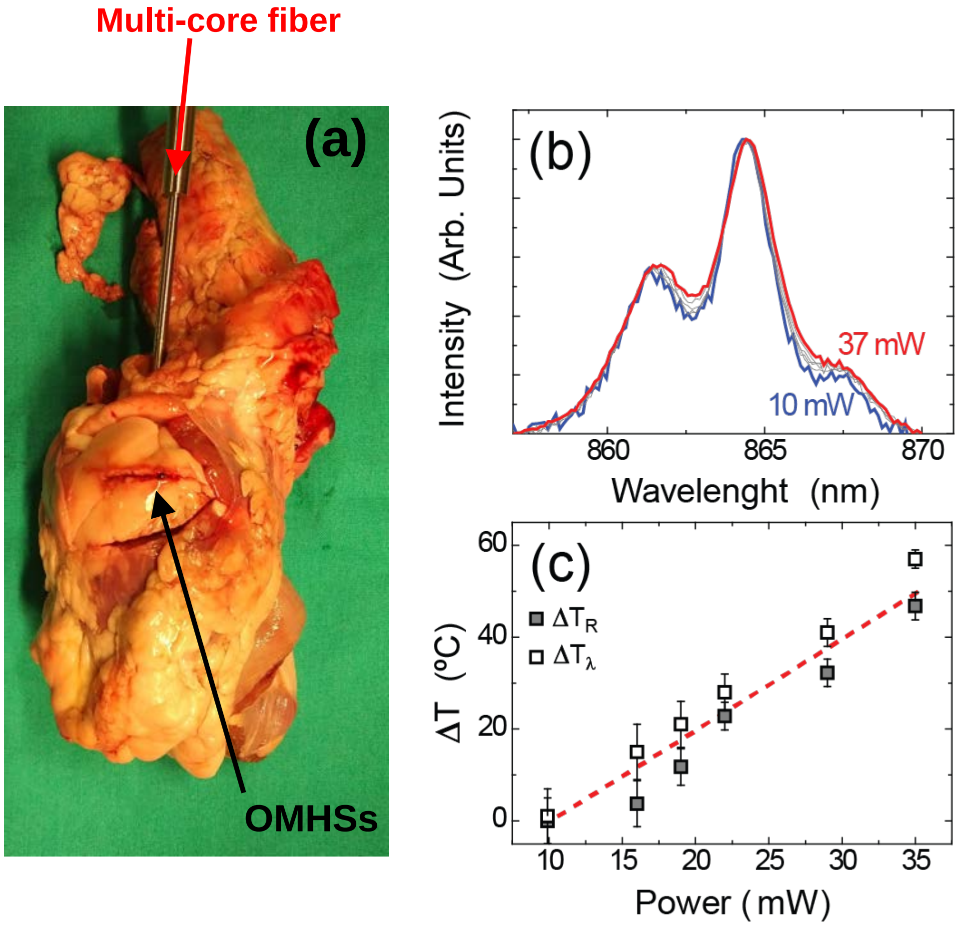

Figure 7. (a) Optical image of the lamb´s heart used for the *ex vivo* experiments. The location of the optical fiber as well as the subtissue injected OMHSs are indicated. **(b)** Emission spectra obtained for different laser powers. **(c)** Temperature increment induced in the subtissue allocated OMHSs as a function of the laser power. Results obtained by using the ratiometric and spectral shift calibration are included. Dots are experimental data and the dashed line is a guide for the eyes.

The combination of magnetic nanoparticles and luminescent nanothermometers through encapsulation with a polymer into optomagnetic hybrid structures achieves in situ control of thermal therapies inside biological tissues. The magnetic and luminescent properties of the constituting nanoparticles are maintained and the robustness of the thermal feedback during photothermal and/or magnetic heating is demonstrated.

Hybrid Materials

D. H. Ortgies,* F. J. Teran, U. Rocha, L. de la Cueva, G. Salas, D. Cabrera, A. S. Vanetsev, M. Rähn, V. Sammelselg, Y. V. Orlosvkii, and D. Jaque

Optomagnetic nanoplatforms for in situ controlled hyperthermia

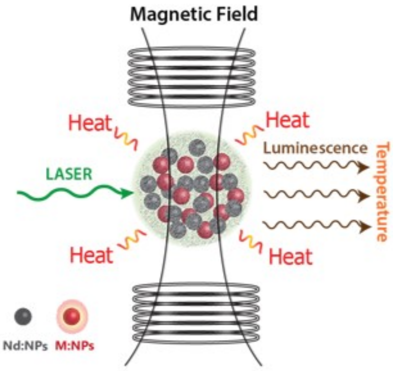

ToC figure ((Please choose one size: 55 mm broad × 50 mm high **or** 110 mm broad × 20 mm high. Please do not use any other dimensions))

Supporting Information

Optomagnetic nanoplatforms for in situ controlled hyperthermia

Dirk H. Ortgies, Francisco J. Teran, Uéslen Rocha, Leonor de la Cueva, Gorka Salas, David Cabrera, Alexander S. Vanetsev, Mikhel Rähn, Väino Sammelselg, Yurii V. Orlosvkii, and Daniel Jaque*

Section S1. Dynamic Light Scattering Studies

DLS measurements were performed in a Zetasizer Nano ZS instrument (Malvern) in a standard 1 cm quartz cuvette on 0.1 mg/ml dispersion of the optomagnetic hybrid structures (OMHS) in water. The energy source was a laser emitting red light, and the angle between the sample and detector is 173°C.

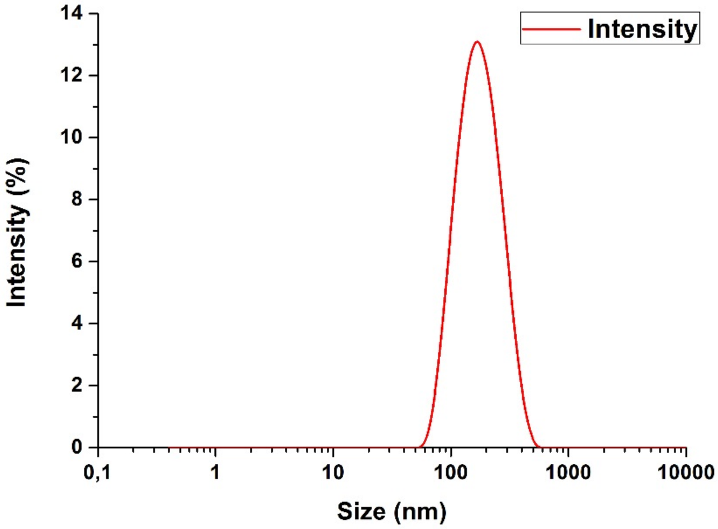

Figure S1. DLS revealed an average hydrodynamic radius of 185 ± 75 nm.

Section S2. Compositional analysis

The Fe and La content of the OMHSs was measured by inductively coupled plasma-optical emission spectrometry (ICP-OES, PerkinElmer Optima 2100 DV ICP) after acidic hydrolysis in aqua regia and dilution in doubly distilled water.

The percent weight of the organic part of the encapsulates (PLGA + coatings) was obtained by thermogravimetric/differential thermal analysis (TGA/DTA) performed on a TA Instruments TGA 500 apparatus, applying a heating rate of 10 °C/min from room temperature to 1000 °C under air. Prior to the analysis, OMHSs were lyophilized to obtain the corresponding powder.

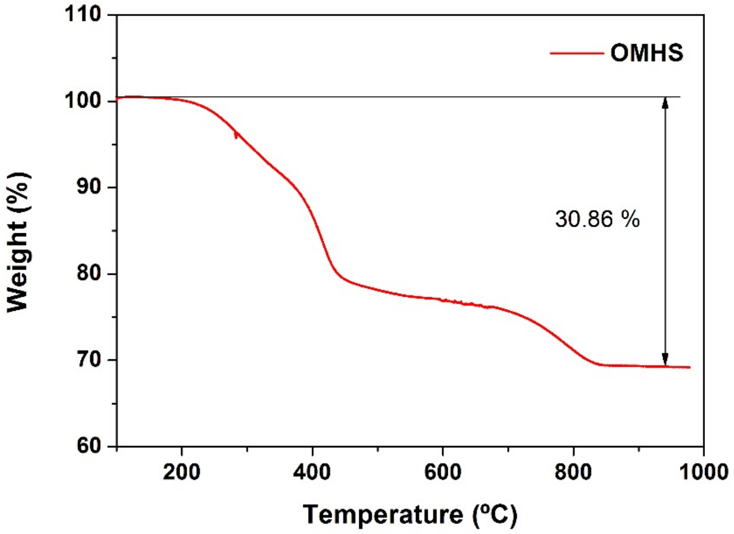

Figure S2. TGA analysis of the OMHS. It reveals that 31 % of the material are organic stemming from the encapsulation with the polymer. This result is in good agreement with an ICP-MS performed on the nanostructures revealing 20 % iron oxide (19.95 % Fe_2O_3) and 50 % LaF_3 (50.85 %).

Section S3. DC Magnetic characterization.

The magnetic characterization was carried out in a vibrating sample magnetometer at room temperature (Lakeshore, Oxford Instrument) by first saturating the sample in a field of 2 T. Saturation magnetization (MS, expressed in emu per g of magnetite, Fe_3O_4) was evaluated by extrapolating the experimental results obtained in the high field range, where the magnetization linearly increases with 1/H.

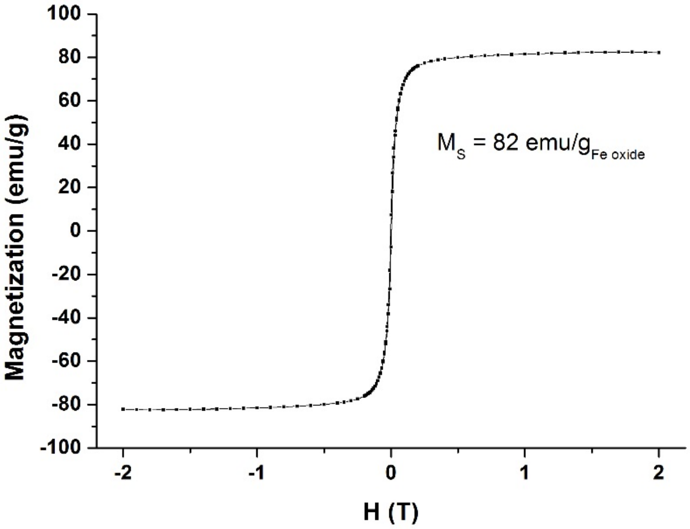

Figure S3. Maghemite mass-normalized magnetization cycles of the OMHSs at room temperature. .

Section S4. Influence of aggregation, viscosity and encapsulation on SAR values

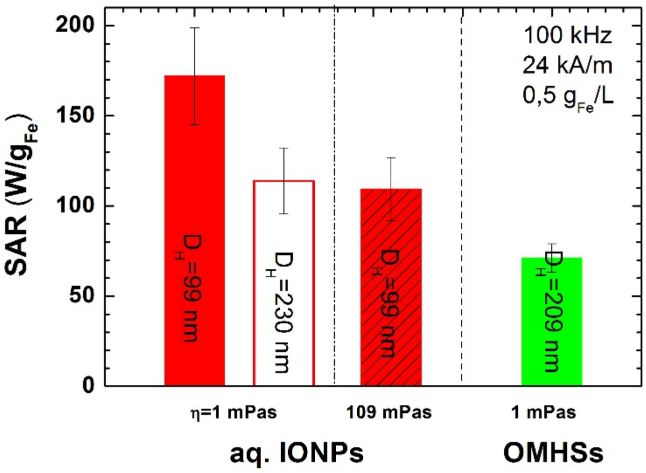

Figure S4. Representation of the aggregation effect on SAR values of DMSA coated IONPs at different hydrodynamic sizes and viscosity values and in OHMSs dispersed in aqueous media under similar field conditions (100 kHz and 24 kA/m) and iron content (0.5 g_{Fe}/L)

Section S5. HRTEM images of LaF_3:Nd nanoparticles and HAADF.

HR TEM analysis of $LaF_3:Nd^{3+}$ nanoparticles synthesized *via* the microwave-hydrothermal treatment of a freshly precipitated gel was performed using a FEI Titan Themis 200 microscope working at 80 kV, equipped with a high-angle annular dark field detector for 200 to 300 kV and the EDX signal was collected with a SuperX SDD (Bruker). The sample was prepared by dropping the colloidal solution of $LaF_3:Nd^{3+}$ nanoparticles in water onto a formvar coated copper grid (3 mm in diameter) followed by the evaporation of the solvent. From the obtained images (**Figure S5**) one can see, that the synthesized sample consists of well defined disaggregated hexagonal-shaped nanoparticles with a diameter of around 15-20 nm. Nanoparticles are very well crystallized; there is no sign of an outer amorphous layer, which frequently can be observed on nanoparticles synthesized *via* “wet” chemical routes like co-precipitation method at elevated temperature. The same instrument was also employed for HAADF measurements of OMHSs in order to obtain the HAADF images shown in **Figure 2** of the article.

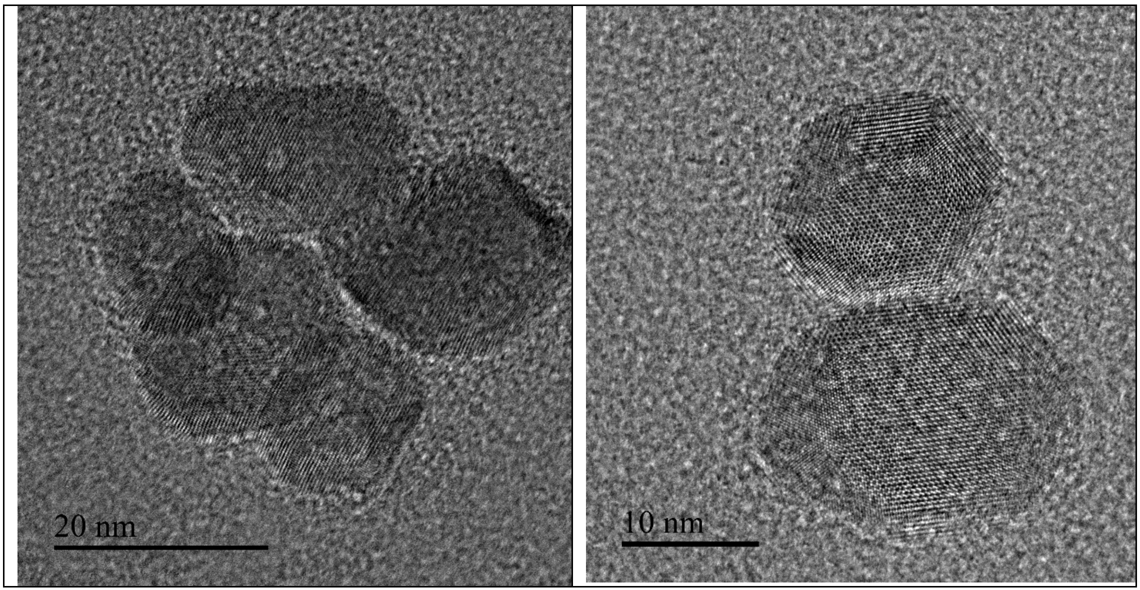

Figure S5. HR TEM images of $LaF_3:Nd^{3+}$ nanoparticles. The nanoparticles are very well crystallized with no sign of an outer amorphous layer.

Section S6.- TEM of OMHS and M:NPs

The TEM image of the OHMS in **Figure 2** of the paper was obtained with a JEOL JEM 1010 microscope operating at 100 kV. The sample was prepared by placing one drop of a dilute suspension in water onto a carbon coated copper grid and leaving it to dry at room temperature. The same instrument and method were used for the TEM image of the IONPs.

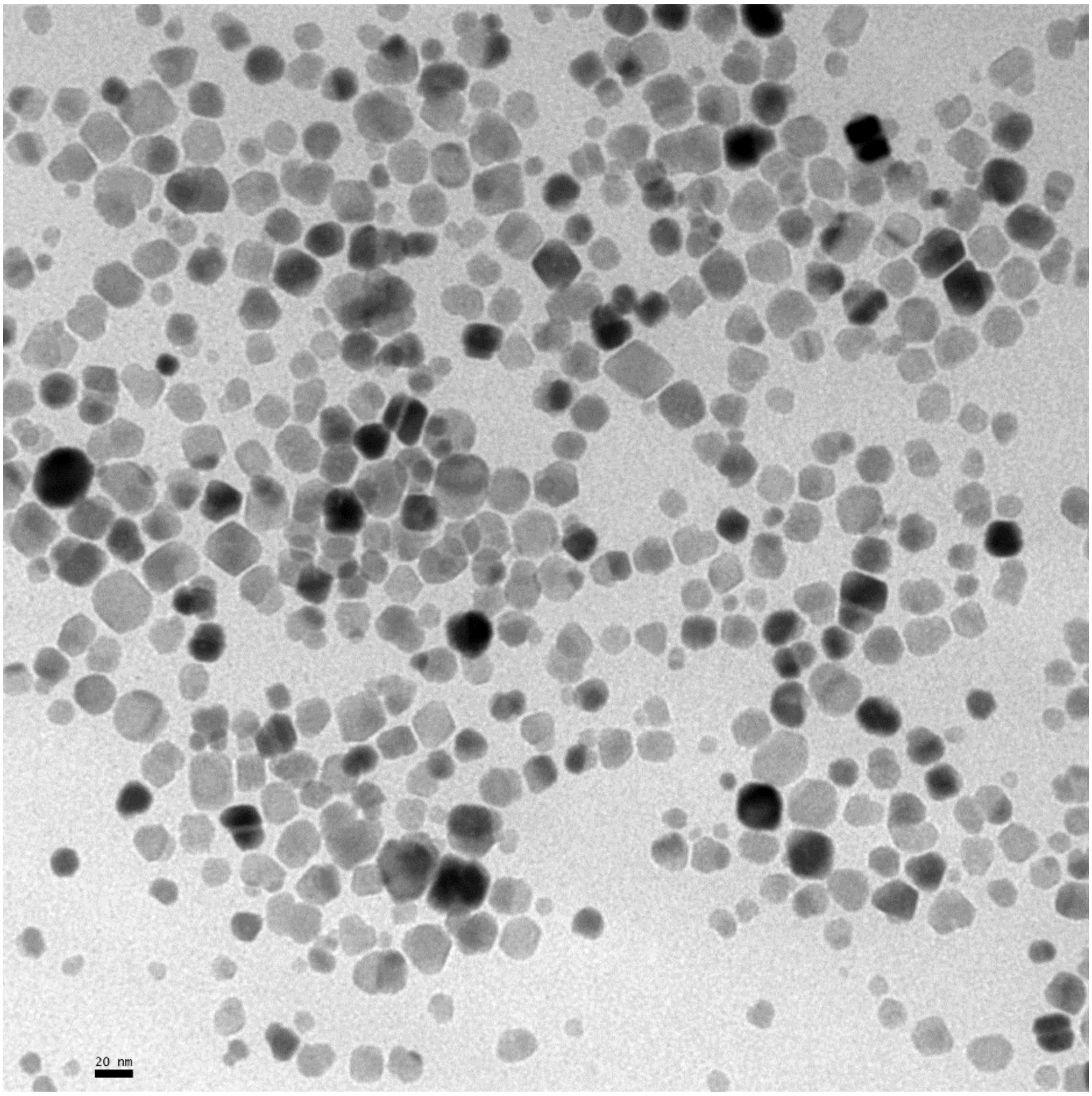

Figure S6. A representative image of the employed IONPs.